Investigation of Corrugated Wing in Unsteady Motion

A. Shahzad[1], H. R. Hamdani[2] and A. Aizaz[†,2]

[1] *Research Centre for Modelling and Simulation, National University of Sciences and Technology, Pakistan*
[2] *Aerospace Engineering Department, College of Aeronautical Engineering, National University of Sciences and Technology, Pakistan*

†*Corresponding Author Email:ahmadaizaz@cae.nust.edu.pk*

ABSTRACT

Delayed stall is the most dominant lift enhancing factor in insect flapping motion. Micro air vehicle operates at Reynolds number 10^4-10^5; slightly higher than the insects' Reynolds number (Re). In the present research, thefocus is to investigate "stall-absent" phenomenon at Re representative of the micro air vehicles, the effect of spanwiseflow on the leading edge vortex and also to study the effect of geometry variations on the aerodynamic performance of the wing in unsteady motion. Corrugated dragonfly airfoil with rectangular wing planform is used, however, with wing kinematics restricted to azimuth rotation only. Three-dimensionalfinite-volume method is used, through commercial software Fluent, to numerically solve time-dependent incompressible Navier-Stokes equations. Computed results at Re 34000 and 100,000 reveal the same phenomenon of delayed stall, as observed in the case of insects. Furthermore, the performance of flat plate, profiled and corrugated wing in a sweeping motion at a high angle of attack is also compared.

NOMENCLATURE

c	mean chord length in meters	y^+	thenon-dimensional length scale associated with a turbulence model
R	wing length (span) in meters		
r_2	radius of the second moment of wing area in meters		
S	wing area in sq meters	$\dot{\psi}_o$	constant angular velocity in (rad/sec)
t_t	total time of pure translation in seconds	Ψ	Azimuth rotation angle
T	non-dimensional time		
U	reference velocity	$\dot{\psi}$	angular velocity of azimuth rotation

1. INTRODUCTION

In general, the Re of insects does not exceed 10,000. According to Wakeling and Ellington (1997), the typical Re of a dragonfly varies from 100 to 10,000. Insects such as a dragonfly, locust and damselfly employ corrugated wings and these corrugations vary along the longitudinal axis flattening out towards the wing tip, as described by Kesel (2000). Although the pleated airfoils may not appear suitable according to the traditional airfoil principles, the experimental studies of Murphy and H. Hu (2010), Newman et al. (1977), Okamoto et al. (1996), Tamai and H. Hu (2008) and Thomas et al. (2004) on the corrugated airfoil in the steady flow or the gliding flight have shown some

encouraging results. The aerodynamic performance of a corrugated airfoil is comparable to a profiled airfoil and a flat plate airfoil at a low Re. According to Rees (1975a) the fluid flowing over the airfoil gets trapped in the corrugation valleys where it either becomes stagnant or rotates slowly, resulting in virtual profiling over the corrugated airfoil. The negative pressure developed in these corrugations contributes to the excessive lift. The CFD analysis of Vargas and Mittal (2004), Vargas et al. (2008), Kim et al. (2009) and Levy and Seifert (2010) are consistent with the findings of the experimental research.

The role of a flapping wing to generate enough lift to stay in the air has been investigated by Weis-Fogh (1973). Ellington (1984) has published

comprehensive research, categorized into six parts, on the aerodynamics of the insect hovering motion. He confirmed Weis-Fogh's observation that most of the hovering animals flap their wings in a horizontal plane but disagreed with the use of quasi-steady flow assumption. The first evidence of a prolonged attachment of the leading edge vortex (LEV) is provided by Maxworthy (1979) on the model of a flinging wing. Dickinson and Gotz (1996) have measured the aerodynamic forces on an airfoil at the Re 100, starting abruptly and showing the enhanced lift due to the LEV but it was limited to 2 to 3 chord lengths due to its shedding. Ellington et al. (1996) have performed a 3D flow visualization study on the actual Hawkmoth flapping in a wind tunnel. These results, coupled with the flow visualization studies conducted on their robotic flapping model of the hawkmoth, showed that the dynamic stall vortex on the wing did not shed during the translational motion of the wing because it was stabilized by a strong spanwise flow. The CFD analysis of a similar situation by Hau Liu *et al.* (1998) and Lan and Sun (2001) have confirmed this 'stall absent' mechanism. The experiments performed by Birch and Dickinson (2001) using a robotic model of a flapping fruit fly at the Re= 70 showed that a small spanwise velocity component exists within the LEV core. They hypothesized that the attenuating effect of the downwash induced by the tip vortex and the wake vorticity limits the growth of the LEV by lowering the effective angle of attack and thus prolonging the attachment of the LEV.

2. THE PRESENT STUDY

In the case of an MAV, the combination of a large length scale and the slightly high flight velocities (around 5-20 m/s) result in the chord Reynolds number range of approximately 104-105 which is higher than the Reynolds number of the flapping wing insects. The Reynoldsnumber is chosen since this Re range has been used in many studies for MAVs such as by Naderi *et al.* 2016).Typical applications of MAV include search and rescue operations, situational awareness in battlefield, aerial surveillance and reconnaissance, sensing biological and chemical agents, sports broadcasting and many more. Tamai and H.Hu (2008) have conducted an experimental study on the bio-inspired airfoil at the Re 34000 and compared it with the GA(W)-1 airfoil and the flat plate with an aim to explore the potential applications of such untraditional airfoils in the MAV design. Through steady state analysis, they concluded that the aerodynamic performance of a bio-inspired airfoil is comparable with its counterparts. The corrugated airfoil produced the maximum lift with comparable drag but most importantly, the flow separation is suppressed causing the delayed stall. In the present study, the work of Tamai and Hu (2008) is extended by focusing on the unsteady motion at the Re 34000. Luo and Sun (2005) studied the effect of the corrugations on the aerodynamic force production of the sweeping model insect wing at a low Re 200 and 3500 at an angle of attack of 40˚. They concluded that the corrugated wing and the flat plate produce approximately the same aerodynamic forces because, for the sweeping motion at larger angles of attack, the length scale of the corrugation is much smaller than the size of the LEV. Although the role of the LEV as a major lift enhancement mechanism at the low Re in insects is well established, its role at a slightly higher Re, representative of the MAV is still to be investigated. Thus, the present study aims at investigating the phenomena of the LEV formation at the Re 34000 and 100,000 and the role of the spanwiseflow in the delayed stall mechanism. Moreover, the effect of the wing geometry on the aerodynamic force production in the sweeping motion is also studied.

3. GEOMETRY AND KINEMATICS

3.1 Airfoil Selection and Wing Geometry

Two types of the airfoil are used in the present study i.e. a triangular wave modelled airfoil and a dragonfly airfoil, as shown in fig. 1.
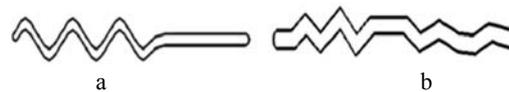

a   b
Fig. 1. a: Airfoil modeled with triangular wave, b: Dragonfly airfoil.

The triangular wave modelled airfoil has a zero camber and its chord length is equal to that of a hawk moth. The parameters are taken from Luo and Sun (2005) and this airfoil forms the basis of the validation. The dragonfly airfoil used in the present study is cambered and has the chord length, the spanwise length and the thickness of the wing as 0.101 m, $3c$ and $0.04c$ respectively. The wing root is offset from the axis of rotation by $0.2c$. Also, note that here 'c' refers to the chord length of the wing. The calculations on a 3D sweeping motion in the MAV regime are performed on the corrugated wing with the dragonfly airfoil, and its parameters are taken from Murphy and Hu (2010).Luo and Sun (2005), while studying the insects with various wing shapes in the sweeping motion, concluded that the wing planform has a minor effect on the force coefficients when the velocity at the radius of the second moment of wing area (r_2) is taken as a reference velocity. As present basic research focuses on the MAVs rather than any particular insect, therefore, for simplicity, rectangular wing planform with constant thickness is used.

3.2 Wing Kinematics

The wing motion is sketched in fig. 2. The flapping cycle of most of the insects can be divided into four phases: downstroke, supination, upstroke and pronation. The wing sweeps back and forth in the upstroke and downstroke phases and is commonly known as translation. However, the wing motion in this paper is restricted to the azimuth rotation (sweeping motion) at a fixed angle of attack,

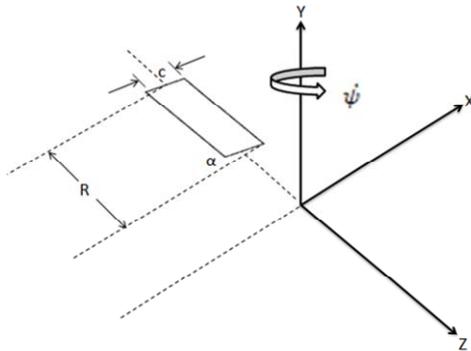resembling an upstroke or a downstroke.

Fig. 2. Motion setup for wing.

More specifically, this paper focuses on the phenomenon of the delayed stall, which is found during the azimuth rotation of the wing i.e. a single stroke / translation only. The wing starts from rest in still air and achieves a constant angular velocity after moving through an azimuth angle of 20°. It is worth mentioning that the duration of the acceleration phase is immaterial in the context of the delayed stall, as confirmed by Hamdani and Naqvi (2010).

The equation for the angular velocity of a wing in dimensional form is given as:

$$\dot{\psi} = (0.5)((\dot{\psi}_o)[1 - cos(\pi t/t_a)]) \quad 0 \le t \le t_a \quad (1)$$

$$\dot{\psi} = (\dot{\psi}_o) \qquad\qquad t > t_a \qquad\qquad (2)$$

In the above equation, $\dot{\psi}_o = U/r_2$ is the reference velocity corresponding to the chord Reynolds number, and r_2 is the radius of the second moment of wing area. Also, t_a is the time taken for accelerating the wing from rest to a constant angular velocity $\dot{\psi}_o$. This time t_a corresponds to the azimuth rotation from 0° to 20°. The total azimuth rotation is restricted to $\psi = 160°$. The radius of the second moment of wing area r_2 is defined as

$$r_2^2 = \frac{1}{S} \int r^2 \, dS = \frac{1}{S} \int_0^R r^2 c \, dr \qquad (3)$$

Where r is the radial distance, S is the wing area and c is the chord length.

4. COMPUTATIONAL METHODS

4.1 Grid Generation

The 2D grid around the airfoil has an O type topology. The whole domain is divided into two O-type portions as shown in fig. 3 (a). This type of division maintains a better resolution near the airfoil and keeps the grid quality parameters under acceptable limit. Fig. 3 (b) provides the side view of the grid distribution on a corrugated wing. For the 3D grid generation; the faces made in 2D are swept in the Z direction to create the volumes.

In order to close the wing tip, a new face is made from the profile of the airfoil at the tip. The wing

itself is not declared as a volume since it requires meshing on its surface only and no calculations are performed inside the wing. This simple sweeping procedure ensures that the grid remains structured throughout, because of the creation of the hexahedral cells. The first grid line is kept as 0.0003 mm from the wing surface. The purpose is to keep y+ around 1 for the calculations involving the turbulence model at a higher Re. A 3D close-up of a corrugated wing is shown in Fig. 4.
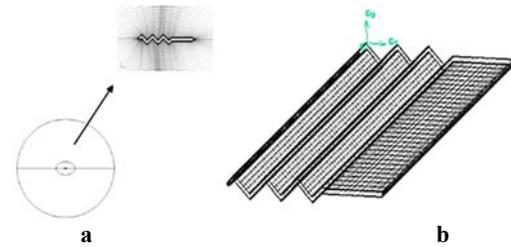

Fig. 3. a) O type grid topology, b) Grid distribution on corrugated wing.
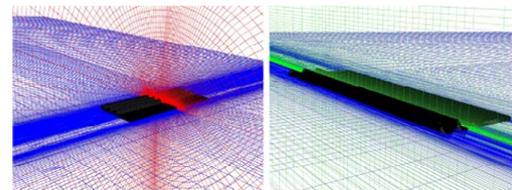

Fig. 4(a) and 4(b). A 3D close up of corrugated wing modeled with triangular wave.

4.2 Computational Setup

A three-dimensional finite volume method, using FLUENT has been used to numerically solve the time-dependent incompressible Navier-Stokes equations by using pressure-based solver. In a pressure-based solver, the governing equations are integrated over the control volumes and algebraic equations with unknown variables are obtained through discretization. These non-linear coupled algebraic equations are solved by an iterative method to achieve convergence. A second order upwind scheme is used for spatial discretization. An implicit formulation is applied and the temporal discretization is limited to the first order accuracy. The pressure-velocity coupling is achieved through pressure implicit with the splitting of operators (PISO) algorithm described by Versteeg and Malalasekera, a highly recommended method for the unsteady calculations. It is a memory efficient algorithm in which equations are decoupled and solved sequentially. The calculations are performed in still air and the wing motion is prescribed through a dynamic mesh feature.

The pressure outlet boundary condition is applied on all the sides of the domain, as it is well suited to the incompressible external flows. The gauge pressure is fixed at zero whereas the other flow parameters are extrapolated from the interior. This
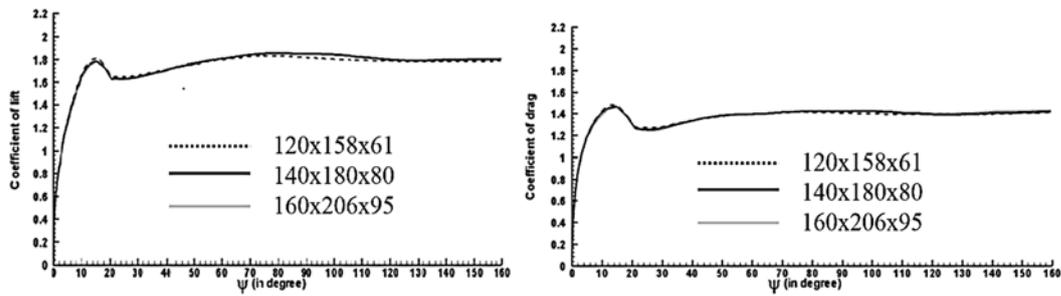
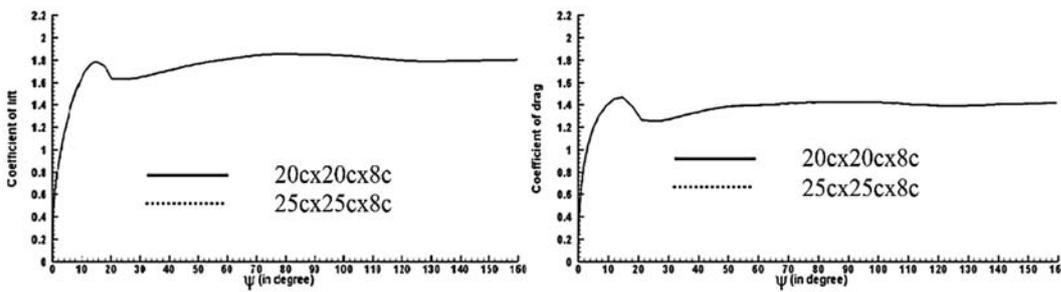Fig. 5. a) Lift coefficient vs ψ. Grid independence, b) Drag coefficient vs ψ. Grid independence.

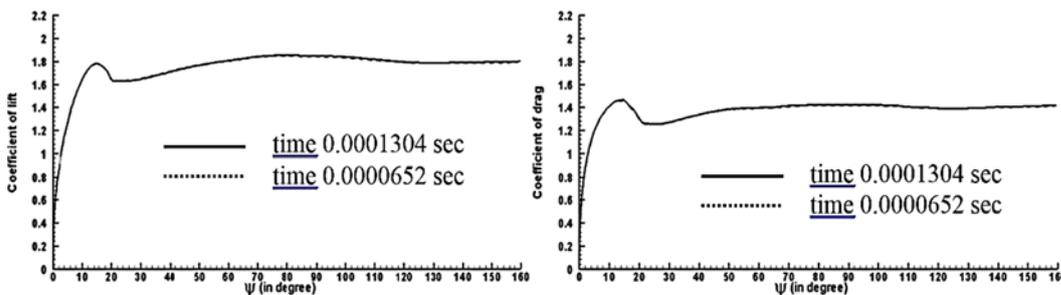Fig. 6. a). Lift coefficient vs ψ. Domain independence, b) Drag coefficient vs ψ. Domain independence.

Fig. 7. a). Lift coefficient vs ψ. Time independence, b) Drag coefficient vs ψ. Time independence.

value of the gauge pressure is relative to the operating pressure of 101325 Pascal set in the "operating condition". At the wing surface, no-slipcwall boundary condition is enforced which means that the fluid on the wall surface will move with the same velocity as the wall. The Spalart-Allmaras (SA) model is used to cater for the turbulence effects. It is a one equation model that solves modelled transport equation for the eddy viscosity. The value of y+ is set around 1 as the SA turbulence model is primarily designed to be used with the meshes that properly resolve the viscous affected region.

5. VALIDATION

5.1 Grid, Domain and Time Step Sensitivity

For the grid independence test, three grids with the dimensions of 120×158×61, 140×180×80 and 160×206×95 (around the wing section, in the normal direction and in the spanwise direction), are chosen. Fig. 5 compares the results of all the grids and it can be seen that the two dimensions of 140×180×80 and 160×206×95 have similar results.

For the domain independence, the domains with

$20c$, $20c$, $8c$ and $25c$, $25c$, $8c$ are tested for the grid dimensions of 140×180×80. The grid independence and the domain independence are both carried out at a dimensionless time step of 0.01. Fig. 6 shows that the domain variation has no effect on the outcome.

In order to make the solution independent of the time step, the dimensionless time ($\Delta\tau=tU/c$) is taken as the reference. The values of $\Delta\tau=0.02$ and 0.01 are used respectively which correspond to 0.0001304 sec and 0.0000652 sec for the Re 34000 and the chord length of 0.101m. The comparison gives a minor difference as evident from fig. 7. The final grid dimensions selected for the calculation is 140×180×80 with the domain extends to $20c$, $20c$, and $8c$.

5.2 Validation of results

The validation part is done on the corrugated rectangular wing with an airfoil modelled with a triangular wave as previously used by Luo and Sun (2005). The final calculations with the grid dimension of 140×180×80, domain size 20c, 20c, 8c and a time step of $1.34×10^{-4}$ seconds, are carried out for the azimuth angle ranging from 0° to 160° at the Re 3500. The results are compared with Luo and Sun (2005) in Fig. 8 which gives a plot of the
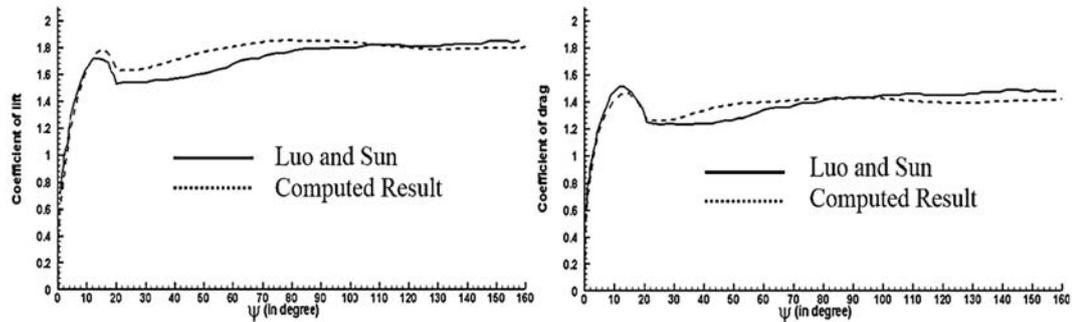
836

Fig. 8. a). Lift coefficient vs ψ. Validation, b). Drag coefficient vs ψ. Validation.
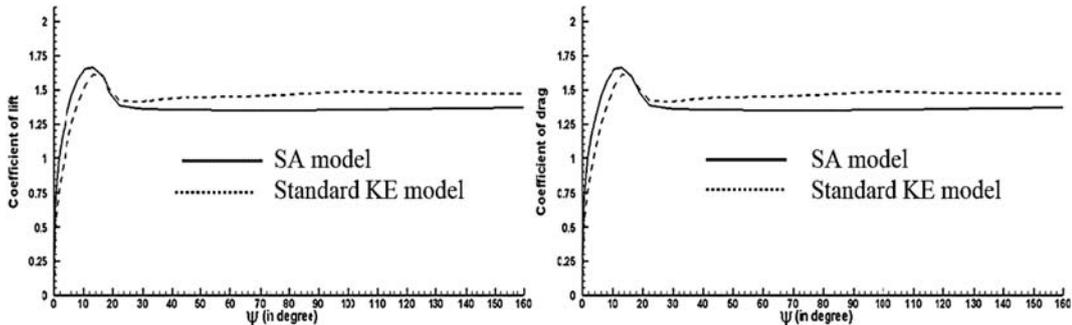

Fig. 9. a). Lift coefficient vs ψ. Turbulence model sensitivity, b). Drag coefficient vs ψ. Turbulence model sensitivity.

aerodynamic force coefficients versus the sweeping angle. The curves of the C_l and C_d are slightly over predictive but the trend remains about the same. A slight difference in the force coefficients is due to the fact that Luo and Sun (2005) used the plan form of the fruit fly whereas in the present study, a purely rectangular plan form is used. The plots give a clear indication of the formation of the leading edge vortex (LEV). This is the phenomenon causing the delayed stall where the LEV does not shed from the wing even after many chord lengths of travel. Owing to the conclusion of Luo and Sun, i.e. the wing planform has a minor effect when the velocity at r_2 is taken as the reference velocity, for simplicity, it is reasonable to use a rectangular wing.

5.3 Turbulence Model Sensitivity

As the validation is carried out at the Re 3500 and the flow at such a low Re is laminar in nature, so there is no need to use the turbulence model. However, the calculations for the MAV applications do involve the Re as high as 1 million where the flow is inherently turbulent and thus needs to use the turbulence model. At the Re 34000,for a dragonfly rectangular wing, the simulations are run with the Spalart-Allmaras (SA) model as well as the standard k-ε model and the results are compared in fig. 9.

The force coefficients for the k-ε model in the steady phase are slightly high. The standard k-ε model is valid for the fully turbulent flows and does not take into consideration the effect of the molecular viscosity. It uses a wall function to model the near wall region. However, the wall function approach is not good in situations where the low

Reynolds number effects are prevalent. Although the SA model requires fine meshing near the walls, at the same time, it properly resolves the viscous affected region. As the SA model is computationally less expensive and is effectively a low Reynolds number model, it is preferred for further calculations.

6. RESULTS AND DISCUSSION

6.1 Effect of Reynolds Number on Formation of Leading Edge Vortex

At the higher angles of attack such as α= 40˚, the flow separation on the suction side of the wing is expected. However, the point of interest is to find out whether there is any sign of vortex shedding during the sweeping motion for the Re corresponding to the MAVs. The aspect ratio (R/c) of the insects generally varies from approximately 2.5 to 5, therefore the R/c= 3 is used in the present study. The aerodynamic force coefficients for the Re 3500, 34000 and 100,000 at the α= 40 degrees are compared in fig. 10. There is a smooth rise in the C_l and C_d in the initial phase when the wing starts from rest and accelerates to reach the peak of the angular velocity. In the unsteady phase, the values of the aerodynamic force coefficients for the Re 3500 remain comparatively lower but as the constant angular velocity is achieved and the stall absent mechanism manifests itself, these values increase and become highest for all the Re. Although, the values of the C_d are slightly low but they are also comparable to the C_l for all the three Re. The values of the C_l for the Re 34000 and
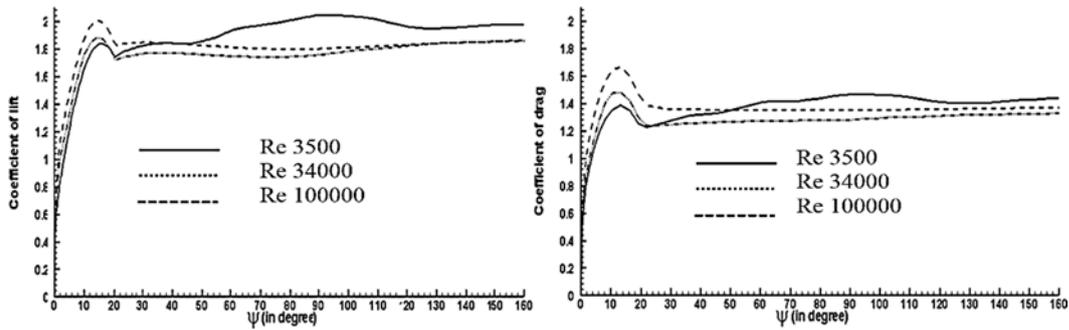
Fig. 10. a). Lift coefficient vs ψ. Effect of Reynolds number, b). Drag coefficient vs ψ. Effect of Reynolds number.

100,000 are almost similar at the end of the stroke, i.e. ψ=160˚, and the strength of the LEV also appears similar. In order to see how the flow behaviour changes with the change in the sweeping angle, the flow picture for the Re 34000 at α= 40˚ on the wing sliced at the 50% span is compared for various values of the ψ in fig. 11 (the flow pictures for the Re 100,000 are similar and thus are not presented here).During the initial acceleration phase, the flow is attached to the surface and trapped in the corrugations of the wing. The first signs of the LEV are seen at ψ=30˚. This LEV is smaller and it continues to grow when the sweeping angle is increased. The flow pictures for ψ=90˚ and 160˚ are similar, which is an indication of the fact, that the LEV has matured and it has occupied the suction side of the wing. There are no signs of vortex shedding.

at ψ=20˚ and 150˚ for the three Re under discussion. There is an indication of a LEV starting to form at the Re 3500 and ψ=20˚. However, the same is not true for the Re 34000 and 100,000 as the flow remains nicely attached to the wing and there is only some flow circulation in the valleys of the corrugations. This means that for the turbulent flow, the onset of the LEV is either slightly delayed or the size of the LEV is so small that it gives an impression of the trapped vortices separated by the corrugation peaks. At ψ= 150˚, the LEV is seen for all the three Re which is consistent with the constant values of the C_l and C_d seen in figure 10. The flow separation region is much larger at the Re 3500 but the LEV is not very stabilized when compared to the Re 34000 and 100,000. This is due the C_l, C_d plots of the Re 3500 having comparatively higher values and some waviness in the curves.
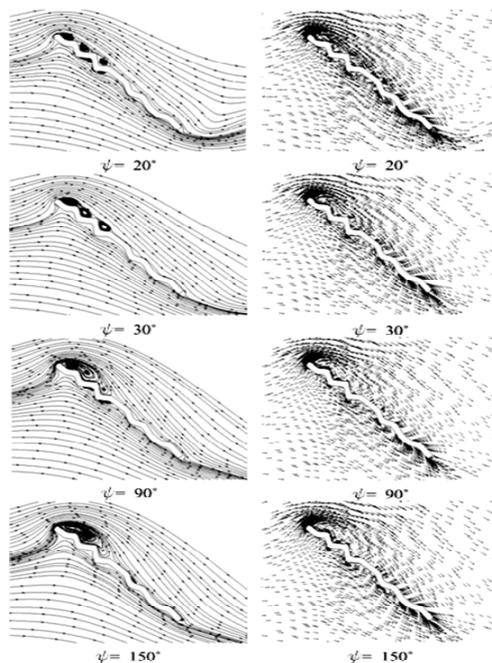

Fig. 11. Stream traces and velocity vectors for different values of ψ (Re 34000 and α=40°).

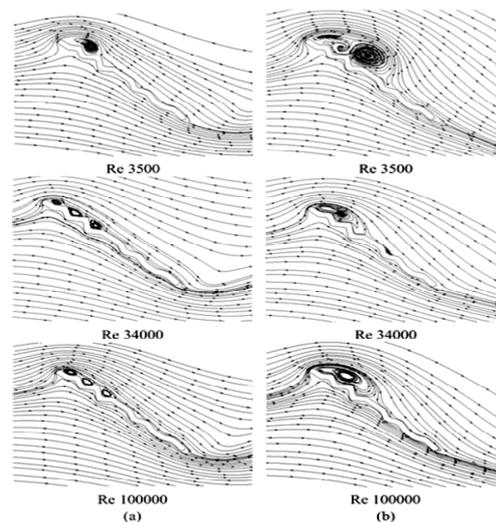Figure 12 gives the comparison of the stream traces

Fig. 12. Stream traces at Re 3500, Re=34000, and Re=100,000 at (a) ψ= 20° (b) ψ= 150°.

The flow over the wing does not remain the same throughout the span as it may encounter forces such as pressure gradients, and centrifugal and coriolis forces. For the present study, the flow pictures at the 25%, 50%, 60%, 70%, 80% and the 90% span (from the root to the tip) are compared for the Re

3500, 34000 and 100,000 at the α=40˚(fig. 13). For the Re 3500, the size of the LEV is very small at the 25% span but increases along the span and the vortex core slightly shifts backward. The flow at the 70% span and beyond gives an indication of the vortex breaking down. For a moderate R/c of 3, as used in this case, the wing tip effects also come into play. The spanwise flow convects the vorticity out towards the wing tip and does not allow the LEV to grow. Then it ultimately bursts and leads to the dynamic stall phenomenon. As has already been mentioned earlier in this paper that the LEV is present on the wing suction side at ψ=150˚ and the same is true for the Re 34000 and 100,000. The flow pictures of the wing sections for the Re 34000 and 100,000 are quite different from those of the Re 3500. For the Re 34000 and 100,000, the size of the LEV is very small at the 25% span and it continues to grow in the spanwise direction. The LEV stays on its position even at the 70% and 80% span and there is no major rearward shift of the LEV core, as seen at the Re 3500. The stream traces at the 90% span are very much different from the other spanwise locations. The absence of the LEV is prominent and from fig. 13 (b), it is confirmed that vortex breakdown has occurred. Hence, it can be inferred for the higher Re that the spanwise LEV break down occurs much closer to the wing tip.
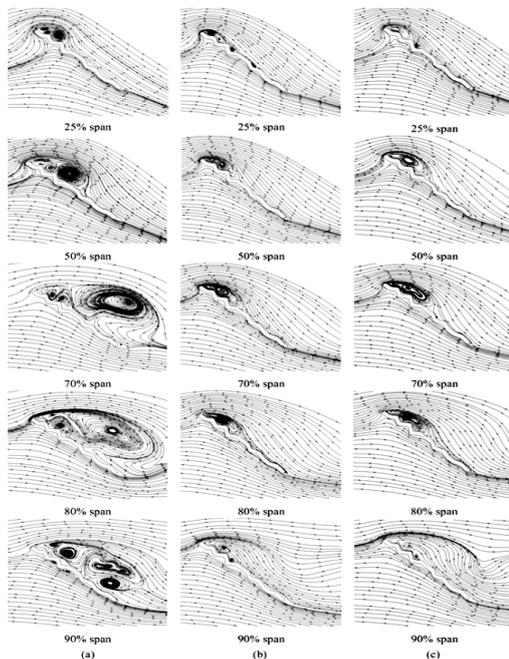

Fig. 13. Spanwise stream traces at (a) Re 3500 (b)Re 34000, and (c) Re 100,000.

6.2 Role of Spanwise Velocity in Delayed Stall

In the insect aerodynamics, the delayed stall is mainly attributed to the spanwise flow over the wing from the wing root to the tip. Fig. 14 shows the spanwise velocity vectors at the core of the LEV for the Re 3500, 34000 and 100,000.

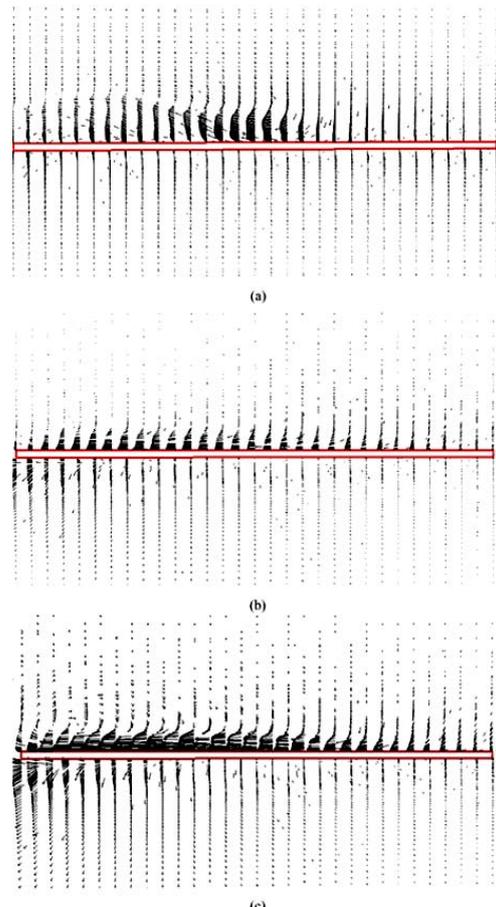An intense spanwise flow is observed from the wing root to the tip.

Fig. 14. Spanwise velocity vectors at the core of LEV. (a) Re 3500 (b) 34000 (c) 100,000.

Figure 15 gives an account of the spanwise velocity distribution at the LEV core. The velocity initially increases and reaches its peak value comparable to the chordwise velocity and then starts to drop near the wing tip.

Table 1 compares the average spanwise velocity to the chordwise velocity related to the Reynolds number. Although the average spanwise velocity is slightly low, the discrete value of the spanwise velocity even crosses the chordwise velocity near the mid-span (Fig. 15). This high value of the spanwise velocity does not allow the LEV to grow, and thus it keeps it firmly anchored to the wing surface. It is due to this reason that the size and stability of the LEV are more robust near the mid-span.

Table 1 Comparison of spanwise and chordwise velocities (in m/s)

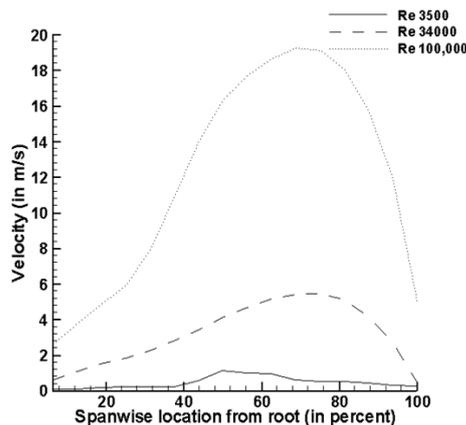|	Re number	Chord wise	Avg Span wise
a	3500	0.506	0.4439
b	34000	5	3.2
c	100000	14.455	12.003

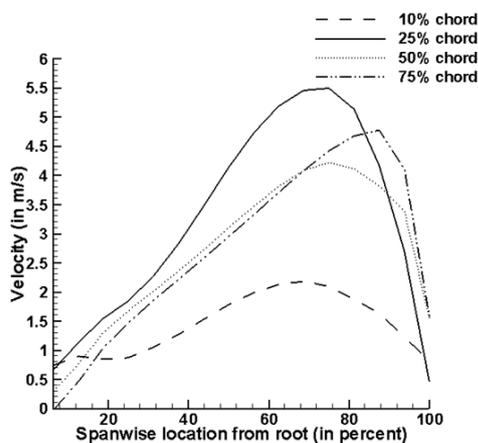**Fig. 15. Spanwise velocity distribution at LEV core for different Re.**

Fig. 16. Spanwise velocity distribution at Re 34000 at different chord lengths.

The velocity profiles near the wing tip are slightly different for the Re 3500 as compared to the Re 34000 and 100,000. The velocity profiles maintain their pattern for almost 80% of the wingspan and this explains why the shedding of the LEV for the Re 34000 and 100,000 is delayed, as shown in fig. 13. At the Re 3500, the spanwise velocity profile near the wing tip has changed dramatically causing the LEV to shed downstream at 70% of the span. In order to analyze the spanwise velocity further, a comparison is drawn at the 10%, 25%, 50% and 75% chord length for the Re 34000 (fig. 16).

The velocity is lowest at the wing root and it increases towards the mid-span. The point of the maximum spanwise velocity for a particular chord length shifts towards the wing tip, moving from 10% chord length to 75% percent chord length. The maximum average spanwise velocity is attained at the 25% chord length and this is the place where the LEV core actually lies.

6.3 Comparison of Azimuth Rotation and Pure Translation

The sweeping motion is compared with the pure

translation at the Re 3500, 34000 and 100,000 at α= 40˚. In case of a pure translation, the velocity is same at all points of the wing along the span. The wing starts from rest and achieves constant linear velocity as it moves in the straight line along the X-axis. In the case of a sweeping motion, the equations for the pure translation are applied in such a way that the time taken for accelerating to a constant linear velocity is the same as the time taken to achieve the constant angular velocity.

The equations for the pure translation are as follows:

$$u = 0.5U[1 - cos(\pi t/t_a)]) \quad 0 \le t \le t_a \qquad (4)$$

$$u = U \qquad t_a \le t \le t_t \qquad (5)$$

Here U is the constant linear velocity. t_a is the time taken for accelerating the wing from rest to a constant linear velocity and t_t is the total time of the translation. Fig.17 compares aerodynamic force coefficients vs time at the Re 3500 and Re 34000, for the two motions under consideration.

It is quite evident that the trend for the higher Re remains the same as seen at the Re 3500. For a pure translation, the LEV sheds into the wake causing the lift and drag to drop as the motion enters the constant velocity phase. The pure translation achieves a higher peak value of C_l and C_d as compared to the sweeping motion. The drop in C_l and C_d for the pure translation at the Re 34000 and 100,000 is much smoother. At the Re 3500, the aerodynamic force coefficients show slight oscillation before decreasing abruptly. Fig. 18 show the stream traces for the pure translation at the Re 3500, 34000 and 100,000. The time instants for the pure translation are chosen in such a way that they correspond to the flow pictures for the sweeping motion given in fig. 11. In the initial phases, when the wing is accelerating to achieve constant linear velocity, the stream traces are very similar to the case of a sweeping motion. At the Re 3500, the LEV is seen on the suction side at 0.27 and 0.34 second and then it sheds into the wake, as evident from the subsequent flow pictures. For the Re 34000, as the time progresses, the LEV starts to appear at t=0.034 second but it then sheds into the wake as seen at the t=0.074 and 0.115 second, causing the lift to drop. The pattern of the vortex shedding for the Re 34000 and 100,000 appears similar, although the time scales are different, owing to the difference in the velocity.

6.4 Comparison of Flat Plate, Profiled and Corrugated Wing AT RE 34000

This section presents the comparison of the flat plate, the profiled, and the corrugated wings for the sweeping motion in the stationary air at the Re34000 and α=40˚. The pictorial view of the airfoils corresponding to the wings is given in fig. 19.
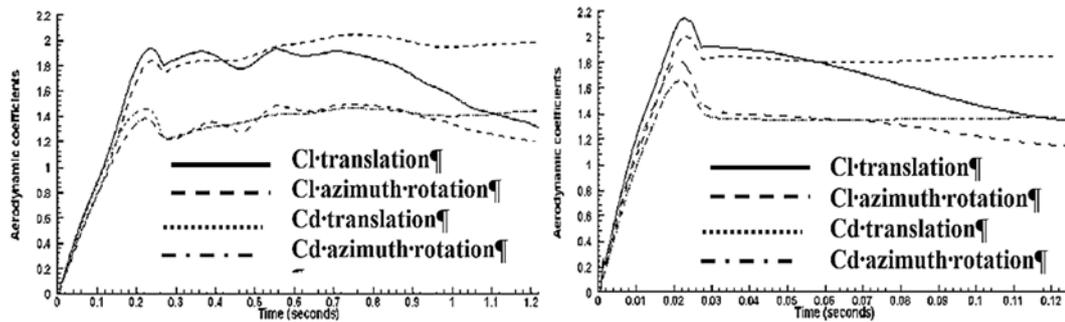
**Fig. 17. a). Force coefficients vs time (Re 3500). Comparison of azimuth rotation and pure translation,
b). Force coefficients vs time (Re 34000). Comparison of azimuth rotation and pure translation.**

Table 2 Aerodynamic force coefficients for flat plate, profiled and corrugated wing

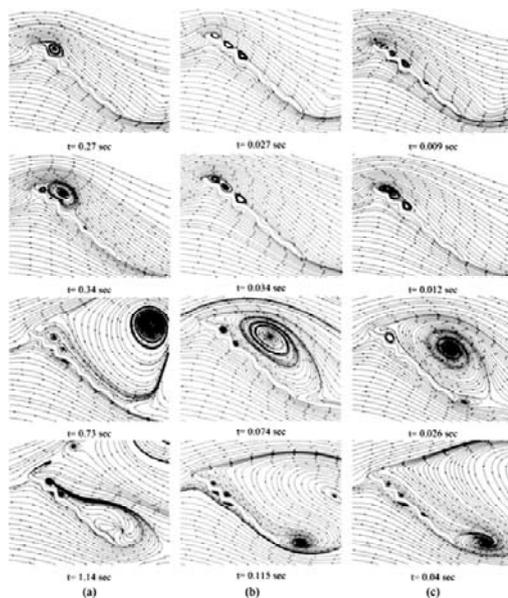|	Wing type	$\overline{C_l}$	$\overline{C_d}$	C_l at $\psi= 150°$	C_d at $\psi= 150°$	$\overline{C_l}/\overline{C_d}$	C_l/C_d
a	Flat plate	1.6896	1.3362	1.8416	1.4101	1.2645	1.306
b	Profiled wing	1.6619	1.1686	1.8119	1.2269	1.4221	1.4768
c	Corrugated wing	1.7047	1.3134	1.8569	1.3707	1.2979	1.3547

**Fig. 18. Stream traces for pure translation at (a)
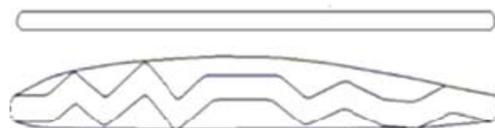Re 3500, (b) 34000, and (c) Re 100,000.**

**Fig. 19. Pictorial view of flat plate, profiled, and
corrugated airfoil.**

The profiled airfoil is a smooth surface that follows the peak of the corrugations. The flat plate has a thickness and a chord length similar to the dragonfly airfoil. The calculations are performed on a wing with a rectangular planform of R/c= 3. The C_l and C_d comparison vs azimuth angle in fig. 20,

show that the pattern of change in the aerodynamic force coefficients and their values are comparable for the flat plate and the corrugated wing, consistent with the conclusion of Luo and Sun (2005) at the Re 3500.The profiled wing produces slightly lower values of the lift and drag under similar conditions.

Table 2 compares the mean value (over the complete sweeping motion) and the steady force coefficients at $\psi= 150°$. The maximum mean C_l and the steady C_l is achieved with the corrugated wing but as the drag for the corrugated wing and the flat plate is higher when compared to the profiled wing, so the profiled wing has a slightly better aerodynamic efficiency in terms of the lift to drag ratio.

The stream traces on the flat plate, the profiled wing, and the corrugated wing in the sweeping motion at the different values of ψ are presented in fig. 21. The pattern of emergence of the LEV and the delayed stall is qualitatively similar. On the flat plate, the LEV is more prominent and the signs of the LEV appearance, in the case of the flat plate are visible very early at $\psi= 20°$. For the corrugated wing, in the initial stages, the flow is trapped in the corrugations and then this flow ultimately contributes and becomes an integral part of the LEV. The size of the LEV on the profiled wing is smallest of all, consistent with the low constant lift seen in fig. 21.

6.5 Effect of Geometry Modification AT RE 34000

In the preceding section, a comparison was drawn between the flat plate, the profiled wing and the corrugated wing in a sweeping motion and it was seen that although the aerodynamic force coefficients may be showing some variation, the overall aerodynamic efficiency is similar. In order to further strengthen this view, different geometric variations of the corrugated rectangular wing are
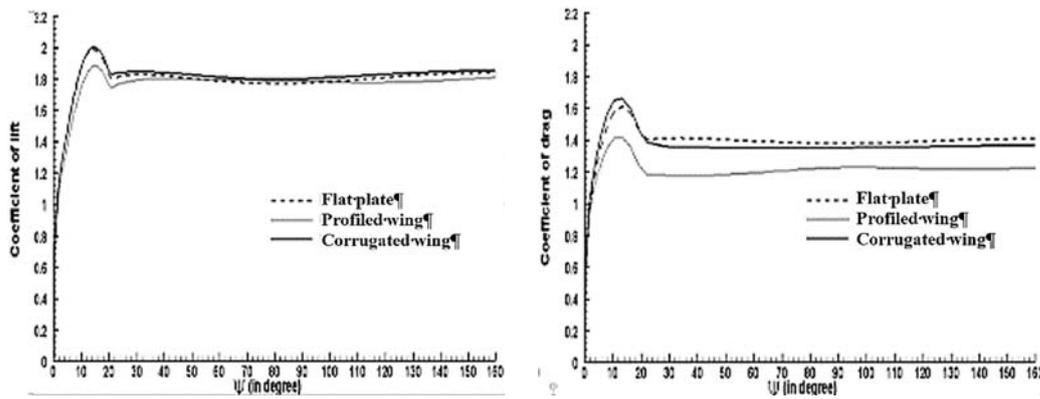
Fig. 20. a). Lift coefficient vs ψ. Comparison of flat plate, profiled and corrugated wing, b). Drag coefficient vs ψ. Comparison of flat plate, profiled and corrugated wing.

Table 3 Comparison of aerodynamic force coefficients for different geometries

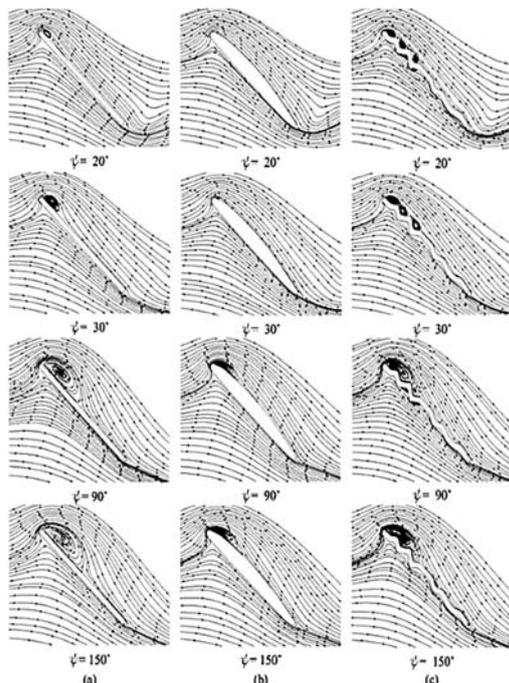|	Wing type	$\overline{C_l}$	$\overline{C_d}$	C_l at ψ=150°	C_d at ψ =150°	$\overline{C_l}/\overline{C_d}$	C_l/C_d
a	Corrugated wing	1.7047	1.3134	1.8569	1.3707	1.2979	1.3547
b	Upper half profiled	1.7219	1.2659	1.8690	1.3294	1.3602	1.4059
c	Upper profiled	1.7443	1.2435	1.8883	1.3011	1.4027	1.4513
d	Lower half profiled	1.7103	1.3084	1.8640	1.3669	1.3072	1.3637
e	Lower profiled	1.6554	1.2542	1.8000	1.3118	1.3199	1.3722

Fig. 21. Stream traces for different ψ.(a)Flat plate (b)Profiled wing (c)Corrugated wing.
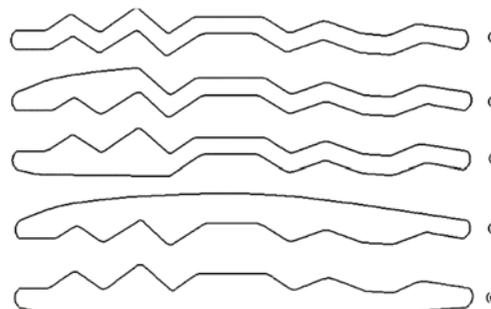

Fig. 22. Geometry modification on corrugated airfoil. (a) Corrugated (b) Upper half profiled (c) Lower half profiled (d) Upper profiled (e) Lower profiled.

tested and their results are compared. The five profiles under the study are presented in fig. 22. The upper half profiled corresponds to the blanking of the first two corrugations on the suction side whereas the lower half profiled means blanking the first two corrugations on the pressure side. The upper profiled has the corrugations only on the pressure side whereas the lower profiled has the corrugations only on the suction side.

The geometric variations show the effect of a number of corrugations on the wing and the effect
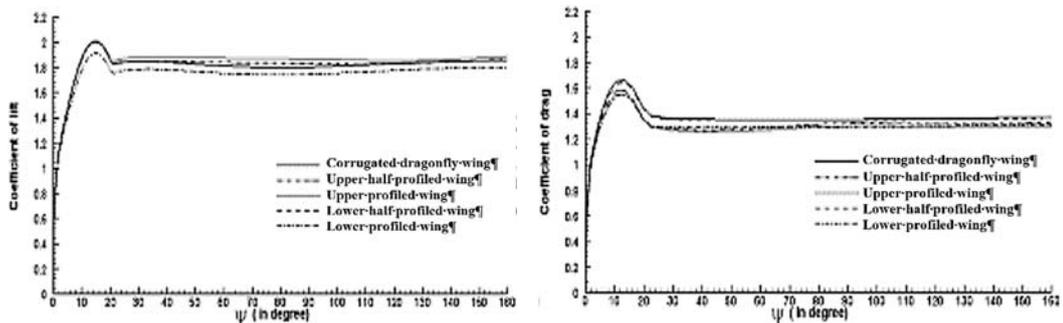
Fig. 23. a). Lift coefficient vs ψ. Effect of geometry modification, b). Drag coefficient vs ψ. Effect of geometry modification.

of increasing the proportion of the profiled surface on the suction side and the pressure side. Blanking the corrugations is equivalent to reducing the number of corrugations on the wing, and at the same time increasing the proportion of the profiled surface. Fig. 23 compares the change in the aerodynamic force coefficients of different geometries during the sweeping motion. Qualitatively, the trend remains the same and the variations in the values remain very small.

values at ψ= 150˚ are compared in table 3 Quantitatively, the upper profiled wing produces the maximum lift and the minimum drag and thus gives a better aerodynamic efficiency. It is worth mentioning that the constant values of C_l and C_d have remained within the range of 1.8-1.8569 and 1.3118-1.3707 respectively. Thus, the variation in C_l and C_d is within 3.16% and 4.49% respectively. Although the corrugated wing produces a slightly higher value of C_d, it partially counters this with a better value of C_l. Fig. 24 shows the stream traces for different wings at the mid-span when the wing has swept to an azimuth angle of ψ= 150˚.

The mean value of C_l and C_d as well as the constant

The LEV is formed in all these cases, with minor variations in the shape and the size owing to the difference in the airfoil shape on the suction side close to the leading edge. The difference of C_l/C_d for the wings under study is so small that the corrugated wing cannot be ignored as a viable option for the MAV design. It will not be wrong to say that the unsteady effect prevails over the geometry and the corrugated wing has no significant aerodynamic shortcomings in the flight range of the MAV. Thus, the structural advantages of the corrugated wing can be utilized to a great extent without compromising on aerodynamic performance. According to Hord and Lian (2012), the corrugations provide the stiffening against the spanwise bending as well as resistance to the bending moment. The corrugations also allow for torsion and development of a camber, as described by Rees (1975b). The corrugated wings are structurally stabilized by folded configurations that increase flexural rigidity to handle the mechanical wear experienced during the flapping motion, as described by Sudo and Tsuyuki (2000).
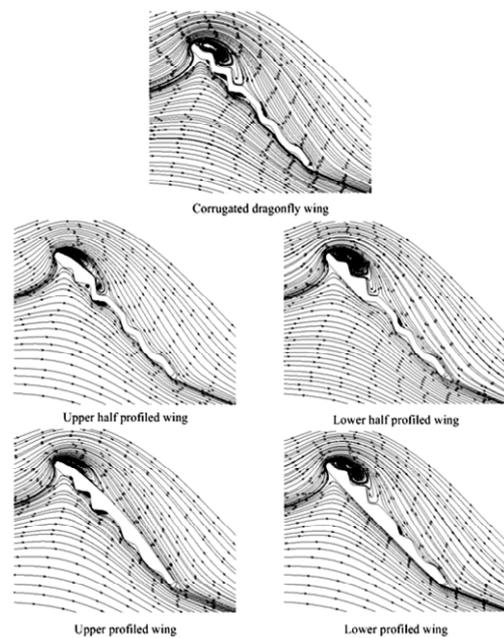

Fig. 24. Stream traces for different geometry variations. (Re 34000, ψ=150° and α= 40°).

7. CONCLUSIONS

The simulation for the corrugated rectangular wing performing unsteady motion at the Re 34000 and 100,000 has been undertaken by solving the incompressible 3D Navier–Stokes equations. Based on the results and their analysis, it is seen that the LEV continues to manifest itself as a lift enhancement mechanism at the Re corresponding to the MAVs. A strong spanwise velocity component from the wing root to the tip is developed which reaches its peak value near the midspan. This maximum velocity achieved is comparable to the chordwise velocity corresponding to the Reynolds number under consideration.

The pure translation motion produces greater peaks of C_l and C_d as compared to the sweeping motion but the "stall absent" is not seen. The leading edge vortex is formed and it then sheds into the wake as the wing continues to move with a constant linear velocity. The results of the flat plate and the corrugated wings for the sweeping motion at the Re

34000 and at high angles of attack give similar outcomes, consistent with the findings of the previous research related to the flapping insects at the Re 3500. A comparison of the flat plate, the profiled, and the corrugated wings in sweeping motion gives only a slight variation in the force coefficients. However, there is no marked difference in their aerodynamic efficiencies. Moreover, the study on different variations of the corrugated profiled wings also suggests that although there is some difference in the force coefficients, the aerodynamic efficiency in terms of the C_l/C_d remains almost unaltered. Hence, the corrugated wing can be used in the MAV design so that its structural advantages can be exploited with no significant compromise on the aerodynamic performance.

ACKNOWLEDGEMENTS

REFERENCES

Birch, J.M., and M. H. Dickinson. (2001). Spanwise flow and the attachment of the leading-edge vortex on insect wings. *Nature*, 412(6848), 729–733.

Dickinson, M. H. and K. G. Gotz. (1996). The wake dynamics and flight forces of the fruit fly Drosophila Melanogaster. *Journal of Experimental Biology* 199, 2085–2104.

Ellington, C. P. (1984). The aerodynamics of hovering insect flight. I-VI. *Phil. Trans. R. Soc.* London B, 305, 1–181.

Ellington, C. P., A. P. Willmott C. Van Den Berg and A. L. R Thomas (1996). Leading-edge vortices in insect flight. *Nature* 384, 626–630.

Fogh, T. W. (1973). Quick estimates of flight fitness in hovering animals, including novel mechanism for lift production. *Journal of Experimental Biology* 59,169-230.

Hamdani, H. R. and A. Naqvi (2010). A study on the mechanism of high lift generation by an insect wing in unsteady motion at small Reynolds number. International *Journal for Numerical Methods in Fluids*, published online in Wiley Inter Science.

Hau, Liu, Charles P. Ellington, Keiji Kawachi, Coen Van Den Berg and Alexander P. Willmott. (1998). A computational fluid dynamic study of Hawk Moth hovering. *Journal of Experimental Biology* 201, 461–477.

Hord, K. and Y. Lian (2012). Numerical Investigation of the Aerodynamic and Structural Characteristics of a Corrugated Airfoil. *Journal of Aircraft* 49(3), 749-757.

Kesel, A. B. (2000). Aerodynamic characteristics of dragonfly wing sections compared with technical aerofoil. *Journal of Experimental Biology* 203, 3125–3135.

Lan, S. L. and M. Sun (2001). Aerodynamic properties of a wing performing unsteady rotational motion at small Reynolds number. *Acta Mechanica* 149, 135-147.

Levy, D. E. and A. Seifert (2010). Parameter Study of Simplified Dragonfly Airfoil Geometry at Reynolds Number of 6000. *Journal of Theoretical Biology* 266, 691-702.

Luo, G. and M. Sun (2005). The Effects of Corrugation and Wing Planform on the Aerodynamic Force Production of Sweeping Model Insect Wings. *Acta Mechanica Sinica* 21(6), 531–541.

Maxworthy, T. (1979). Experiments on the Weis-Fogh mechanism of lift generation by insects in hovering flight. Part 1. Dynamics of the fling. *Journal of Fluid Mechanics* 93, 47-63.

Murphy, T. and H. Hu. (2010). An Experimental study of a Bio-inspired corrugated airfoil for micro air vehicle applications. *Exp Fluids* 49, 531-546.

Naderi, A., M. Mojtahedpoor and A. Beiki (2016). Numerical investigation of non-stationary parameters on effective phenomena of a pitching airfoil at low Reynolds Number. *Journal of Applied Fluid Mechanics* 9(2), 643-651.

Newman, B. G., S. B. Savage and D. Schouella (1977). Model test on a wing section of a dragonfly. In *Scale Effects in Animal Locomotion*. (ed. T. J. Pedley) 445–477. London: Academic Press.

Okamoto M., K. Yasuda and A. Azuma (1996). Aerodynamic characteristics of the wings and body of a dragonfly. *Journal of Experimental Biology* 99, 281–294.

Rees, C. J. C. (1975a). Aerodynamic properties of an insect wing section and a smooth airfoil compared. *Nature* 258:141–142.

Rees, C. J. C. (1975b). Form and function in corrugated insect wings. *Nature* 256, 200–203.

Sudo, S. and K. Tsuyuki (2000). Wing morphology of some insects. *JSME Int J C* 43, 895–900.

Tamai, M. and H. Hu. (2008). A Bio-inspired Corrugated Airfoil at Low Reynolds Numbers. *AIAA Journal of Aircraft* 47(6), 2068-2077.

Thomas, Alr, G. K. Taylor, R. B. Srygley, R. L. Nudds and R. J. Bomphrey (2004). Dragonfly flight: free-flight and tethered flow visualizations reveal a diverse array of unsteady lift-generating mechanisms, controlled primarily via angle of attack.

Journal of *Experimental Biology* 207, 4299–4323.

Vargas A., R. Mittal and H. Dong. (2008). A computational study of the aerodynamic performance of a dragonfly wing section in gliding flight. *Bioinspir.Biomim* 3, 026004.

Vargas, A. and R. Mittal (2004). Aerodynamic Performance of Biological Airfoils. *2nd AIAA Flow Control Conference,* Portland, OR, AIAA 2004-2319.

Versteeg, H. K. and W. Malalasekera. *An introduction to computational fluid dynamics,* *the finite volume method*, second edition, Pearson Education.

Wakeling, J. M. and C. P. Ellington (1997). Dragonfly flight. I. Gliding flight and steady-state aerodynamic forces. *Journal of Experimental Biology.* 200, 543–556.

Won-Kap K., J. H. Ko, H. C. Park and D. Byun. (2009). Effects of Corrugation of the Dragonfly Wing on Gliding Performance. *Journal of Theoretical Biology* 260(4), 523-530.